International Journal of Multiphase Flow 197 (2026) 105635

Contents lists available at ScienceDirect

International Journal of Multiphase Flow

journal homepage: www.elsevier.com/locate/ijmulflow

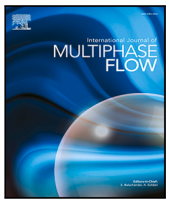

Research Paper

Cavitation onset in counter-rotating vortices from separating disks

Mariana Costa [a,b,*], Tom van Terwisga [b], Daniele Fiscaletti [b], Jerry Westerweel [a]

[a] Process & Energy Department, Delft University of Technology, Mekelweg 2, Delft, 2628 CD, Delft, The Netherlands
[b] Maritime and Transport Technology Department, Delft University of Technology, Mekelweg 2, Delft, 2628 CD, Delft, The Netherlands

ARTICLE INFO

Keywords:
Cavitation
Vortices
PIV
Pressure reconstruction

ABSTRACT

In tribonucleation, a liquid-to-gas phase transition induced by a local pressure drop (cavitation) is highly undesirable, as it causes surface erosion and noise. A paradigmatic flow characteristic of tribonucleation problems is the flow between two coaxial disks. The flow is produced by the rapid upward movement of the top disk, which is initially at rest and in contact with the bottom disk. An analytical model, the so-called negative squeeze film, is typically used to predict the flow in the gap between the disks in this class of problems. Such a model considers an azimuthally uniform inflow in the gap between the disks. In this study, we experimentally show that if a negligibly small misalignment between the axes of the two disks is introduced, the inflow is not azimuthally uniform as expected from the negative squeeze film, but an entry jet appears in the flow between the disks. This entry jet is associated with the formation of two counter-rotating vortices. From reconstructing the pressure field from PIV velocity data in the vortex regions, we find that the local pressure is lower than the vapor pressure. This indicates that the gaseous phase in the cores of the vortices, which is observed from shadowgraphy visualizations in our study, should be attributed to cavitation. The negative-squeeze-film model, however, largely fails to predict the minimum pressure. Therefore, the onset of cavitation is not correctly captured by the analytical model.

1. Introduction

Cavitation is a multiphase phenomenon that occurs when the local pressure of a liquid decreases below a critical pressure, typically deemed as the vapor pressure (Franc and Michel, 2005). The local pressure drop, often induced by high flow velocities or accelerations, leads to a phase change, and, consequently, to the formation of vapor bubbles, which can evolve into stable cavities. When collapsing, these pockets of vapor emit noise, and can cause erosion and vibrations to nearby surfaces. Examples of harmful effects of cavitation encompass a wide range of disciplines (Braun and Hannon, 2010), from maritime technology, with propeller cavitation (Melissaris et al., 2020; Ghasemnezhad and Roohi, 2024), to medical sciences, with increasing evidence that cavitation inside the brain is associated to traumatic brain injury during sudden impacts (Kurosawa et al., 2009; Adhikari et al., 2016); from biology, with the snapping shrimp stunning or killing its prays through cavitating bubbles (Versluis et al., 2000), to energy conversion, with cavitating blades in turbomachineries (Arndt, 1981).

An archetypal flow where cavitation is observed to occur is the flow resulting from the rapid diverging movement of two solid surfaces that are initially in contact. In the gap between such separating surfaces, cavitation bubbles can appear, which can develop into stable vaporous cavities. This flow is found in tribology, where two closely opposed surfaces are separated by a thin film of liquid. Examples are seat valves, gears, dampers, and bearings, among many other mechanical components (Resch and Scheidl, 2014; Ertas and Delgado, 2018; Yoshizumi et al., 2018). Here, opposing surfaces resist separation until a critical point, where they then rapidly separate, creating gas cavities. This phenomenon is known as stiction, from a combination of "static" and "friction" for historical reasons, although the problem is apparently highly dynamic (Roemer et al., 2015; Wang et al., 2020). Several investigations have focused on the modeling of the stiction force in the presence of cavitation, the so-called Stefan problem (Stefan, 1875; Scheidl and Gradl, 2016). Sobhi et al. (2023) demonstrate how non-Newtonian fluid behavior and permeability influence pressure distribution, flow characteristics, and formation of cavitation regions between porous disks. The flow in a transient squeeze film was studied by Lang et al. (2019), who proposed an experimental approach to examine a fast-developing flow in a thin fluid gap. However, the precise knowledge of the flow development in the thin film between the surfaces remains elusive, particularly in relation to cavitation onset and development.

Another example of divergent surfaces producing cavitation can be found in human joints, leading to the common joint cracking sound.

* Corresponding author.
E-mail address: M.DeOliveiraBarraCosta@tudelft.nl (M. Costa).

https://doi.org/10.1016/j.ijmultiphaseflow.2026.105635
Received 2 October 2025; Received in revised form 23 January 2026; Accepted 28 January 2026
Available online 29 January 2026

The most studied joint cracking is that of the metacarpophalangeal joint, resulting in what is commonly referred to as the cracking of knuckles. Different theories have been postulated to try to explain the knuckle cracking sound (Kawchuk et al., 2015). Some attributed it to the collapse of the cavitating bubbles formed in the articulation, while others identified cavitation inception as the mechanism leading to cracking noise, consistent with tribonucleation (Chen and Israelachvili, 1991). However, tribonucleation does not explain the magnitude of the sound of knuckle cracking, which is much larger than that measured from other experiments of tribonucleation. The recent study by Chandran Suja and Barakat (2018) provides further support for bubble cavitation as the main mechanism explaining joint cracking. In their model, tribonucleation remains, however, essential in initiating joint cavitation by producing the cavitation bubbles that later collapse. Consistently, evidence shows that with an initial (at rest) spacing greater than 1.4 mm the joint cannot be cracked (Unsworth et al., 1971). The structure of the multi-phase flow inside the synovial joint when the knuckles are cracked is unknown, though. Specifically, the mechanism leading to the onset of stable cavities remains unclear. Moreover, the flow topology of the thin film that is characteristic of tribonucleation is rather unexplored to date. This problem can be approached by investigating the archetypal flow obtained from solid disks that after being initially in contact undergo a rapid mutual separation.

While the macroscopic flow structure of tribonucleation has been investigated scarcely, comparatively more interest has been devoted to the instabilities of viscous liquids confined between two plates of variable geometries under traction, determining the so-called 'lifted Hele-Shaw cell' (Hele-Shaw, 1898). Here, the edge of a sample drop destabilizes from its initial, regular shape through the Saffman-Taylor mechanism (Saffman and Taylor, 1958). Air fingers protrude towards the center of the sample, generating the characteristic fingering pattern. Poivet et al. (2003) experimentally found a relationship between the stiction force and the onset of cavitation bubbles inside the viscous drop, which was observed to manifest for traction velocities greater than 15 μm s^{-1}. The formation and collapse of individual cavitation bubbles confined in thin films of the order of nanometers have also been observed in recent experiments, such as in Moffatt et al. (2021) and Combriat et al. (2024). In the latter study, the area of the bubbles presented an inverse scaling with respect to their lifetime. The curvature radius of the top diverging surface was also found to play an important role in the size of the bubbles that are generated. Geike (2020) provides a literature review of cavitating bubble dynamics modeling for negative squeeze motion, emphasizing the coupling of the Reynolds and Rayleigh–Plesset equations to resolve tensile stresses and transient effects during the separation of lubricated circular plates. These studies focus on microfluidic phenomena, where the flow is dominated by viscosity, and for which the process of formation of the observed cavitation bubbles is well understood and described. It remains, however, unclear what the flow behavior would be for increasing separation heights between the plates, when the phenomenon becomes dominated by inertia.

This work aims at characterizing the flow structure in the thin film between two coaxial circular plates, which, initially in contact, undergo a rapid divergent movement. In the experimental setup, the plates are negligibly misaligned, mimicking thus the operating conditions in real tribonucleation problems. For the largest values of velocities and accelerations, stable cavities are observed to form. The results of the experimental analysis are compared with the analytical model, the so-called negative squeeze film.

This paper is structured as follows. The experimental setup is described in Section 2.1. Section 2.2 introduces the correlation averaging method, which enhances the spatial resolution of the velocity vector field and accuracy. In Section 2.3, the methodology to reconstruct the pressure field from particle image velocimetry (PIV) is illustrated. In the same section, the simplifications applied to the Navier–Stokes equation to perform such a reconstruction are detailed. An analytical solution for flow behavior in the ideal case of having perfectly parallel disks, referred to as the negative squeeze film, is reported and illustrated in Section 2.4. The section on the results (Section 3) begins with a characterization of the four studied cases based on cavitation strength and the velocity of the diverging disk, using shadowgraphy images, in Section 3.1. An explanation for the non-uniform azimuthal flow and the formation of the two counter-rotating vortices is given in Sections 3.2 and 3.3. In Section 3.4, velocity profiles are compared between experiments with non-uniform inflow and theoretical predictions assuming uniform inflow. A discussion on possible definitions of a cavitation number for this problem is included in Section 3.5. In Section 3.6, the influence of the vertical velocity on pressure reconstruction is assessed in comparison with the horizontal component. Section 3.7 presents the results related to velocity, vorticity and pressure for the four cases. Finally, the conclusions are summarized in Section 4.

Table 1
Characterization of the four cases under study with respect to the maximum acceleration (a_{max}) and maximum velocity of the diverging disk (v_{max}), time to reach maximum acceleration (t_a) and maximum velocity (t_v), gap height between the disks when the diverging disk reaches the maximum acceleration (h_a) and maximum velocity (h_v), and time between the disks when the diverging disk reaches its final position (t_p).

	a_{max} (m s^{-2})	v_{max} (m s^{-1})	t_a (ms)	t_v (ms)	h_a (mm)	h_v (mm)	t_p (ms)
Case 1	30	1.1	94	114	11.2	31.9	140.2
Case 2	60	1.6	56	71	11.7	31.3	85.2
Case 3	78	1.8	47	60	11.7	32	72.1
Case 4	96	2	39	50	11.7	30.3	62

2. Materials and methods

2.1. Experimental setup

The experimental setup consists of two coaxial disks that are initially at rest, mutually at contact. Actuated by a pneumatic cylinder (Festo model DZH-32-50-PPV-A), the top disk moves vertically along the common axis, reaching maximum accelerations larger than 90 m s^{-2}. Four pressure values are set in the compressed-air system, i.e., 2.0 bar, 3.5 bar, 4.5 bar, and 6.0 bar, which determine the four cases under investigation in this work, referred to as Case 1, 2, 3 and 4, respectively. A thorough description of these four cases is reported in Table 1.

The disks are placed in a 50 × 50 × 30 cm^3 tank filled with water. The flow developing in the gap between the two disks, which results from their rapid separation, is known as the negative squeeze film, and it is particularly important in lubrication studies (Reynolds, 1886). As mentioned in the Introduction, the disks are imperceptibly misaligned. The rapid diverging movement in combination with a lack of perfect parallelism of the top disk with respect to the bottom one determines the formation of a non-uniform jet flow at the interface between the disks, which produces two counter-rotating vortices. The circulation around these vortices strengthens for increasing acceleration of the top disk; see Table 1; the acceleration is determined by the pressure in the compressed air system that drives the piston. These aspects are analyzed and discussed in further detail later in the paper.

Two techniques of flow investigation are applied in this research to investigate the flow phenomena, i.e. shadowgraphy and particle image velocimetry (PIV). For the first technique, a LED panel is located behind the tank, serving as the light source that passes through the transparent disks and cavities until it reaches the sensor of one of the CMOS cameras. As for the PIV, a second camera records the displacement of the particle images. The water is seeded with fluorescent orange polyethylene microspheres having a diameter between 75 μm and 90 μm, which act as tracer particles. The tracer particles are fluorescent and absorb

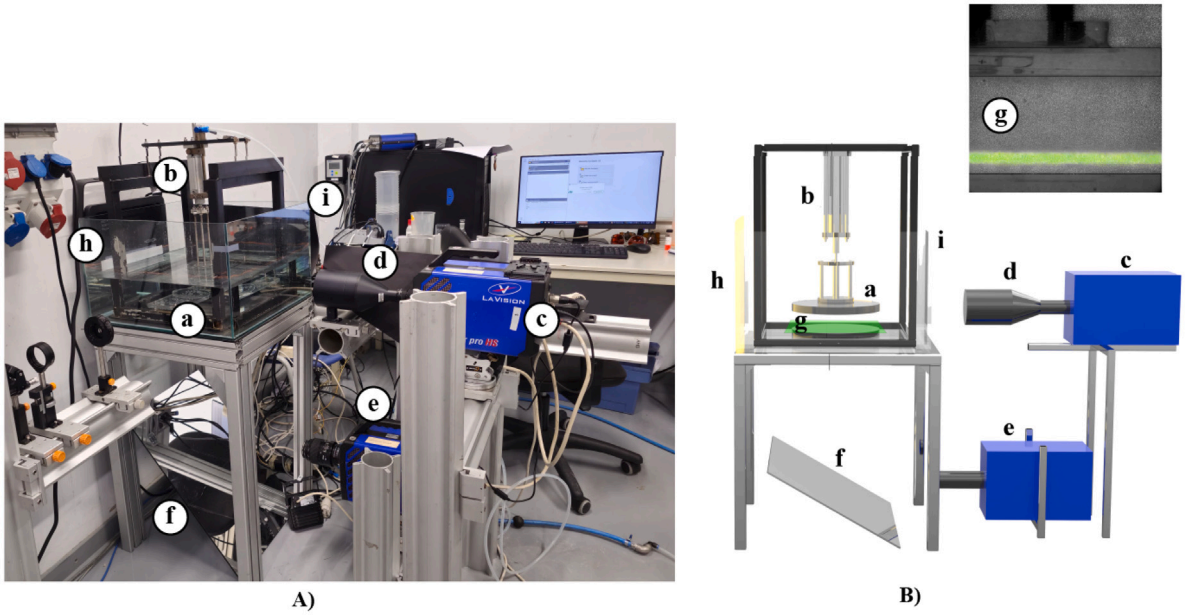

Fig. 1. Photo (A) and Schematic (B) of the experimental setup. a: disks; b: pneumatic actuator; c: high-speed camera for shadowgraphy; d: telecentric lens; e: high-speed camera for PIV; f: mirror; g: laser sheet; h: LED panel; i: glass tank.

Table 2
The experimental conditions for the PIV measurements.

Seeding	
Type	Fluorescent orange polyethylene microspheres
Diameter (μm)	75–90
Illumination	
Source	Nd:YLF
Sheet thickness (mm)	3.1
Energy (mJ)	30
Recording	
Sensor type	CMOS
Frame rate (Hz)	1146
Lens type	105 mm focal length
Image magnification	0.113
f-number	2.8
Field of view (mm^2)	145 × 141
Resolution (px mm^{-1})	10.28
Post-processing	
Window size (px^2)	8 × 8
Window overlapping	50%
Vector spacing (mm)	0.4

the green laser light, which is emitted as orange fluorescent light. A dual-cavity laser creates a light sheet perpendicular to the axes of the two disks. It is worth mentioning that a long-pass filter is positioned in front of the camera lens, transmitting mainly the light scattered by the fluorescent particles to the camera sensor, therefore increasing the signal-to-noise ratio of the measurements. Detailed information on the PIV measurements can be found in Table 2. A schematic of the experimental setup is shown in Fig. 1.

Regarding the pre-processing of the PIV images, inhomogeneous lighting introduces low-frequency noise, which can be eliminated using a high-pass filter. This filter preserves the particle movements while suppressing low-frequency background noise and unwanted reflections like the ones generated by the cavities (Sciacchitano and Scarano, 2014). For this reason, a high-pass filter (Thielicke and Stamhuis, 2014) is applied to the particle images, and a reduction in the percentage of spurious vectors from 3.01% to 2.34% is obtained for an interrogation window of 16 × 16 px.

The images are acquired using commercial software (Davis 10, LaVision GmbH). A code written in LabVIEW (National Instruments) enables the automatic triggering of the image acquisition and the movement of the top disk to occur in parallel. The displacement between the two disks, and, consequently, the velocity and acceleration, are estimated by imaging analysis of the shadowgraphy sequences on the vertical plane. The appropriate time difference between the two frames for the cases under analysis (see Table 1) is determined to be of 160 μs for Case 1, 100 μs for Case 2, 80 μs for Case 3, and 80 μs for Case 4. When shadowgraphy is used solely, the frame rate is 2289 Hz, which is the maximum achievable frame rate for a field of view of 66 × 64 mm^2. In the object plane, 1 mm corresponds to 10.28 pixels, for the PIV recordings and 22.61 pixels for the shadowgraphy images, defining the spatial scale of the images.

A telecentric lens is used for shadowgraphy recordings because of its more precise measurement characteristics due to the constant magnification and depth of field, which results in low image distortion and field curvature (Konrath and Schröder, 2002; Erinin et al., 2023). Appropriately adjusting the lens position with respect to the horizontal axis is necessary to place the depth of focus exactly where the vortices are expected to appear. In relation to the PIV setup, a 105 mm focal length lens is used with 2.8 f-number and a 0.113 magnification. The laser sheet is positioned parallel to the disks, approximately 3.6 mm above the bottom disk. This has the aim of reconstructing the velocity vector field at the beginning of the raising movement of the top disk, when the flow acceleration is the largest.

2.2. Correlation averaging

Ten repetitions are conducted for each pressure value of the pneumatic cylinder, resulting in a total of forty acquisitions. We follow the approach of Pennings et al. (2015) who used correlation averaging, or sum of correlation, to enhance the spatial resolution of the velocity field around a vortex. Correlation averaging and sum of correlation refer to the same mathematical operation since correlation averaging is the sum of the instantaneous correlation integrals divided by the number of samples (Meinhart et al., 2000; Westerweel et al., 2004).

The advantages of using correlation averaging arise from the high repeatability of the phenomenon. Therefore, this post-processing technique is applied to the time-resolved correlation maps. Simultaneously,

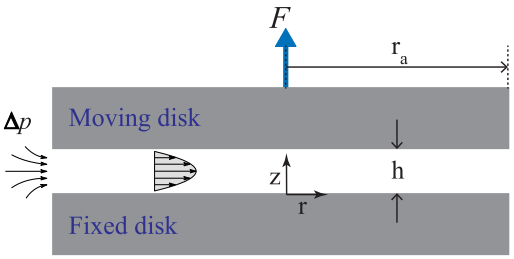

Fig. 2. The parameters characterizing the negative squeeze film are the radius r_a of the disk, and the gap h between the fixed disk and the moving disk. The moving disk is pulled upwards by a force F. For a small gap width $h \ll r_a$ the radial velocity u_r has a parabolic profile Eq. (2). At the inlet there is an additional pressure drop Δp (Hori, 2006).

shadowgraphy images are acquired alongside the PIV recordings, allowing for the selection of PIV image frames that correspond to the gap height h between the two disks in each repetition, to be used in the correlation averaging. This process is automated by a custom-developed code.

With the defined curve of the gap height h between the two disks as a function of the frame for each repetition, the frames associated with the previously estimated gap height are selected, enabling the correlation averaging to be performed.

Double-frame PIV is later carried out, and, from applying correlation averaging as mentioned above, an interrogation window size of 8 × 8 px is obtained, leading to a vector spacing of approximately 0.4 mm for a 50% window overlapping.

2.3. Pressure estimation from PIV data

The pressure field p is reconstructed from PIV data in the region where the vortices occur, by solving the Poisson equation for the kinematic pressure $P = p/\rho$ and incompressible flow ($\nabla \cdot \mathbf{u} = 0$):

$$\nabla^2 P = -\nabla^2 k + \nabla \cdot (\mathbf{u} \times \boldsymbol{\omega}), \tag{1}$$

where ρ is the fluid density, $k = \frac{1}{2}(u^2 + v^2 + w^2)$ the kinetic energy, $\mathbf{u} = (u, v, w)$ the velocity, and $\omega = \nabla \times \mathbf{u}$ the vorticity. We assume two-dimensional flow, i.e. $u^2 + v^2 \gg w^2$ and $\omega = (0,0, \omega_z)$; this assumption is validated in Section 3.6. The vortices are embedded in an irrotational flow, and we select the boundary of the domain to be irrotational, and use $P = \frac{1}{2}(u^2 + v^2)$ as the boundary condition for P. It is worth noting that disregarding the terms related to the z direction leads to an overestimation of the pressure. When the vortex structure is stretched due to the upward movement of the diverging disk, the cross-section of the vortex shrinks. Consequently, the angular momentum conservation dictates that the rotation rate must increase, resulting in a decrease in pressure inside the vortex core.

2.4. The negative squeeze film

The negative squeeze film represents the theoretical prediction of a uniform flow between perfectly parallel and coaxial disks. The analytical model resulting from this prediction can be derived using the Navier–Stokes and continuity equations in cylindrical coordinates, with the appropriate simplifications. The complete derivation is given by Hori (2006).

For a small gap width $h \ll r_a$ the radial velocity u_r is given by a parabolic profile in the z direction:

$$u_r = \frac{3r\dot{h}}{h^3}\left(z^2 - hz\right), \tag{2}$$

as shown in Fig. 2, with: $\dot{h} = \mathrm{d}h/\mathrm{d}t$. The fluid velocity u_z in the z direction is given by:

$$u_z = -\frac{\dot{h}}{h^3}\left(2z^3 - 3hz^2\right). \tag{3}$$

Table 3
The experimental conditions for the shadowgraphy measurements.

Illumination	
Source	LED panel
Recording	
Sensor type	CMOS
Frame rate without PIV (Hz)	2289
Frame rate with PIV (Hz)	1146
Lens type	Telecentric
Lens image scale	0.274
Image	
Field of view (mm^2)	66 × 64
Resolution (px mm^{-1})	22.61

The liquid pressure inside the gap, accounting for fluid viscosity, is

$$p = \frac{3\mu\dot{h}}{h^3}\left(r^2 - r_a^2\right) - \Delta p, \tag{4}$$

where $\Delta p \approx \frac{1}{4}\rho r_a^2(\dot{h}/h)^2$ is the pressure drop due to the converging flow entering between the disks (Hori, 2006). The expression in Eq. (4) is valid for a small gap width $h \ll d$, and ignores inertial terms (Hori, 2006). The pressure given by Eq. (4) is used as a reference, although the condition of small gap width is not strictly valid. Hence, the liquid pressure inside the gap is directly proportional to the viscosity μ and the velocity of the moving disk $\dot{h}$, and inversely proportional to the cube of the gap width, h. Additionally, the pressure distribution in the radial direction has a parabolic shape, with the smallest pressure occurring at the centerline of the disks.

3. Results

In the previous sections, the theoretical background for modeling the flow between perfectly parallel disks was presented. The experimental methodologies for characterizing the flow phenomena, including shadowgraphy and particle image velocimetry, have been illustrated too. Additionally, the technique used to reconstruct pressure fields from the 2D velocity vector fields obtained from PIV have been detailed.

This section presents the results from experimental investigations across the four cases analyzed, each identified by cavitation strength, velocity, and acceleration of the moving disk. We explore the formation of an entry jet and the two counter-rotating vortices. Moreover, we compare experimental non-uniform velocity data with theoretical uniform velocity predictions. A discussion follows on the definition of a possible cavitation number to describe this flow problem, accompanied by an analysis of the influence of the vertical flow component relative to radial velocity on pressure reconstruction. Flow characterization is further expanded by examining velocity vector fields and out-of-plane vorticity. We then discuss the sensitivity of pressure reconstruction to PIV window size.

3.1. Characterization of investigated cases

Shadowgraphy images at different time instants are displayed in Fig. 3 for the four cases (for further information on the kinematic characteristics of these cases, see Table 1). The shadowgraphy recording is used to estimate the gap height h between the two separating disks, the velocity $\dot{h}$ and the acceleration $\ddot{h}$ of the moving disk with the aid of image processing techniques. The diverging disk reaches its final position when $h_{max} = 50$ mm. The time t was defined using the frame rate of the camera, which is 2289 Hz, see Table 3. The complete video for Case 4 is provided in the Supplementary Content, along with the time instants and graphs showing the velocity $\dot{h}$ and the acceleration $\ddot{h}$ of the moving disk as a function of the gap height h. Concerning the occurrence of cavitation, no cavitating vortices form for Case 1; see Fig. 3a to 3f. As for Case 2, shown in Fig. 3g to 3l, only the left vortex

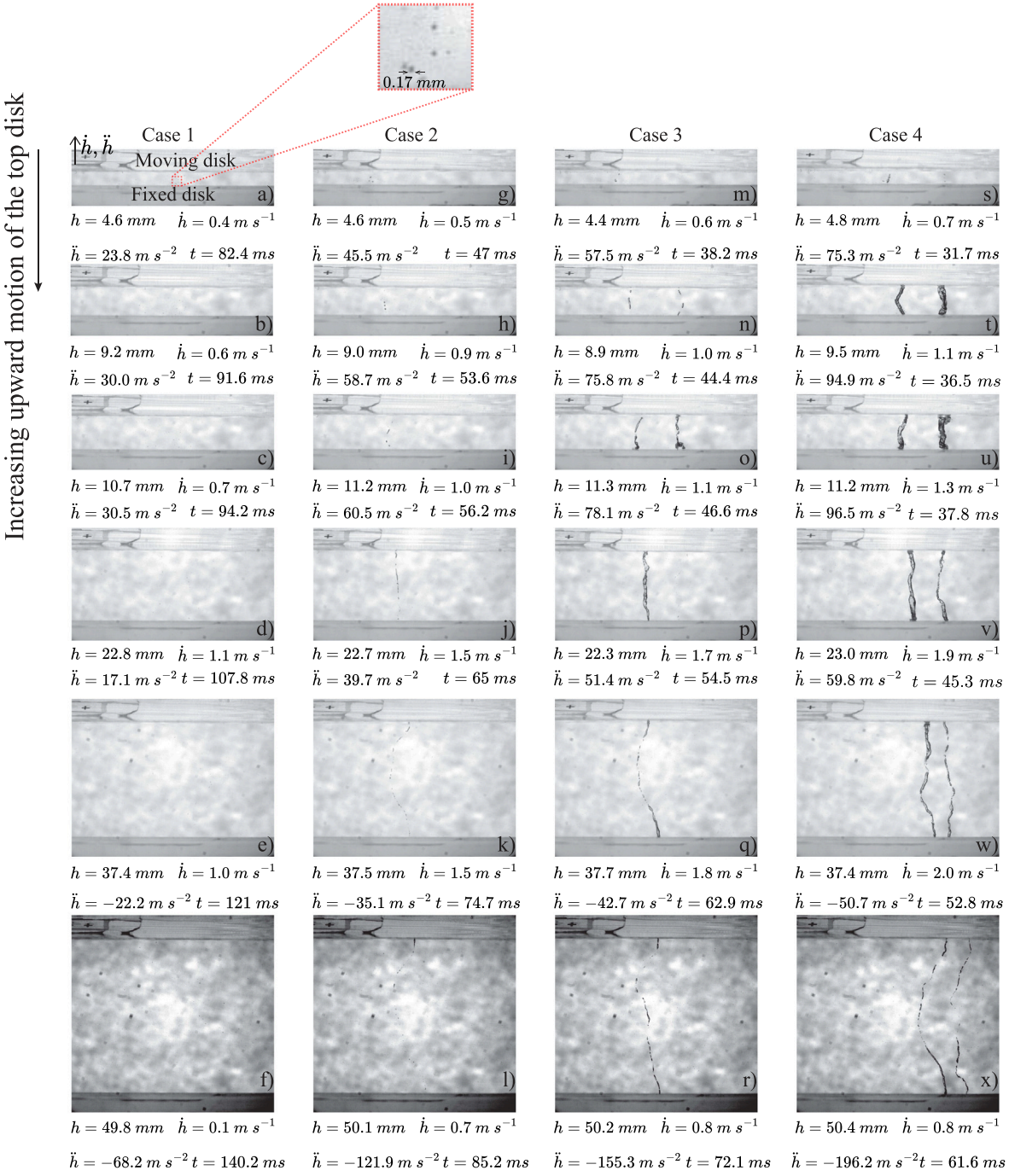

Fig. 3. Shadowgraphy images at different time instants and corresponding to the four different cases detailed in Table 1. Each row shows different instants t, gap heights h between the two separating disks, velocity $\dot{h}$ and acceleration $\ddot{h}$ of the moving disk.

cavitates. Both vortices cavitate once the maximum acceleration a_{max} is equal or higher than 78 m s^{-2}, i.e. for Cases 3 and 4; see Table 1. However, for the former, the right cavity collapses faster than the left one, and the diameter of the cavities is relatively smaller compared to the latter.

Bubbles having a diameter of approximately 0.17 mm can be observed in the gap between the two disks, immediately after the top disk detaches from the bottom one (see Fig. 3a). They possibly originate from small crevices in the surface of the disks (Franc and Michel, 2005). The observed bubbles exhibit a spiraling motion inside the two vortices before being trapped inside their cores (Kelly et al., 2021); see Fig. 3g, 3m and 3s. The appearance of bubbles in this phase is a shared feature between all cases. The size of the two vortex cavities increases when the top disk reaches the maximum acceleration. For Case 3 and 4, the bubbles trapped inside the left vortex gradually grow in size until they form the observed cavity, whereas the bubbles trapped inside the right vortex do not vary significantly in size, and the onset of the right cavity occurs abruptly. From observation of the corresponding shadowgraphy images, Case 1 does not exhibit any vortex cavities, but tiny bubbles following a cylindrical path can be seen in each of the two vortex cores.

The vortex cavities can be either produced by the coalescence of free non-condensable gases in the form of bubbles or be the result of a cavitation process. Evidence that cavitation is the reason behind the appearance of the vortex cavities is that they appear for an acceleration

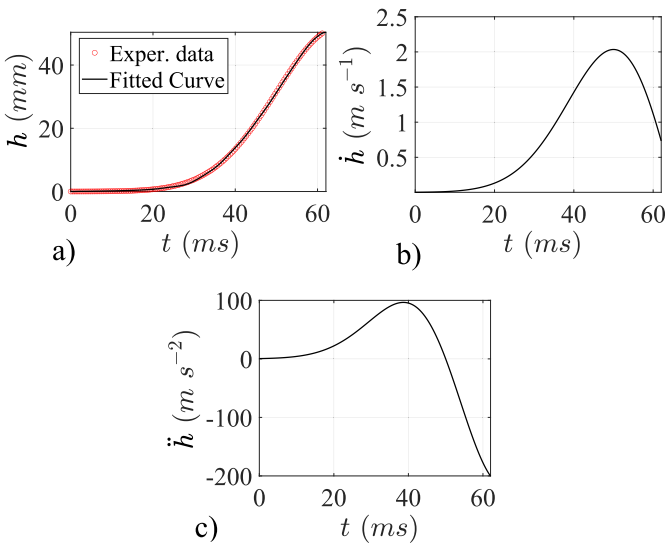

Fig. 4. Displacement h of the moving disk relative to the fixed disk as a function of time is displayed in (a). The red circles represent data points obtained from shadowgraphy recordings, while the black line represents the exponential curve fitted to the data. Velocity $\dot{h}$ of the moving disk with respect to the fixed disk as a function of time is presented in (b). This plot is obtained by differentiating the exponential curve fitted to the data points shown previously in (a). Acceleration $\ddot{h}$ of the moving disk in relation to the fixed disk as a function of time is exhibited in (c). This plot is obtained by differentiating the exponential curve $\dot{h}(t)$ depicted in (b)

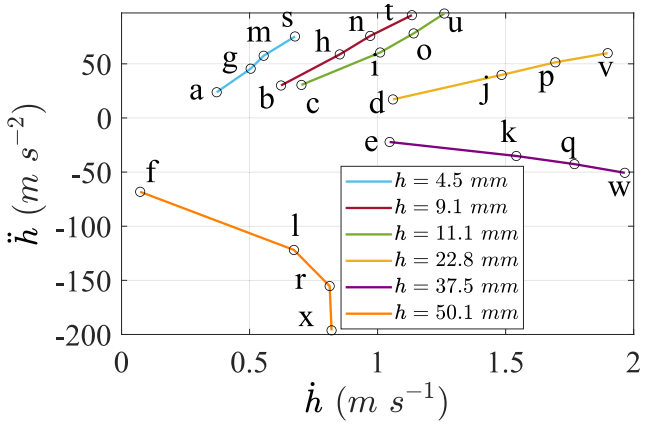

Fig. 5. The velocity $\dot{h}$ and acceleration $\ddot{h}$ of the moving disk for five different gap heights h are represented in the above figure. The circles and letters correspond to the instants shown in Fig. 3.

of the diverging disk of 60 m s^{-2}, i.e. in Case 2, but they do not appear for an acceleration of 30 m s^{-2}, i.e. in Case 1. This is because the circulation produced by the vortices in the latter case may not be sufficiently large to induce a pressure drop in the cores of the vortices, such to induce locally a pressure lower than the vapor pressure.

As mentioned previously, the gap height h between the two separating disks is estimated using image processing techniques applied to the shadowgraphy recordings. This is achieved by selecting a distinct pattern on the moving disk and another on the fixed disk and then employing cross-correlation to each image to determine the relative displacement of these patterns. The gap height between the two disks is then defined based on the relative positions of these patterns. Thus, with the gap height h and the time derived from the frame rate of the camera, it is possible to fit a function to the data points (Fig. 4a). The graph shown in Fig. 4a is associated to Case 4. The same procedure is applied to the other three cases. A suitable function for describing the gap height h as a function of time appears to be:

$$h = c_1 \exp\left(-\left(\frac{t-c_2}{c_3}\right)^2\right) \tag{5}$$

where c_1, c_2 and c_3 are fit constants. An initial gap height $h_0 = h\ (t = 0)$ is required to avoid a diverging pressure $p \to -\infty$ in Eq. (4). We find that $h_0 \cong 0.06\ \ \mu$m – 7 μm; this value of h_0 corresponds to the typical surface roughness of the material of the disks.

The root mean-square errors (RMSE) of the fitting are in the order of 10^{-4} m. To estimate the velocity $\dot{h}$ and acceleration $\ddot{h}$, Eq. (5) is differentiated once and twice, respectively, resulting in Eqs. (6) and (7) shown below.

$$\dot{h} = -\frac{2c_1(t-c_2)}{c_3^2}\exp\left(-\left(\frac{t-c_2}{c_3}\right)^2\right) \tag{6}$$

$$\ddot{h} = \frac{c_1 \exp\left(-\left(\frac{t-c_2}{c_3}\right)^2\right)}{c_3^4}\left(4(t-c_2)^2 - 2c_3^2\right) \tag{7}$$

The velocity $\dot{h}$ and acceleration $\ddot{h}$ can also be expressed as a function of h, which facilitates the comparison between the four cases (Fig. 5). The circles and letters in Fig. 5 correspond to the shadowgraphy images shown in Fig. 3. It is important to note that cavitation inception coincides with the point of maximum acceleration of the top disk, $\ddot{h}$, rather than with its maximum velocity, $\dot{h}$, which when cavitation inception occurs is half of its maximum value.

3.2. The formation of the two counter-rotating vortices

The flow developing in the thin film between the disks is investigated with planar PIV, where the measurement plane is at 3.6 mm height from the bottom disk. Transparent plane disks are used in the experimental setup to ensure optical access to the flow in the gap, therefore enabling the use of PIV. The flow time evolution is presented in Fig. 6. The gray circles depict the positions of the disks, while the green and blue arrows indicate the instantaneous 2D velocity vector field. The first frame, which is taken at approximately 74.1 ms after the separation of the two disks (presented in Fig. 6b) shows that the small angle between the two disks — occurring in a real-case scenario — triggers the generation of a strong entry jet. This is tagged with a red arrow. The order of magnitude of the angle is in tenths of degrees and is estimated from the Shadowgraphy images. The formation of the two counter-rotating vortices (Fig. 6g) occurs following the entry of the non-uniform radial jet flow. The development of this non-uniform jet flow is illustrated from Fig. 6c to 6f at time intervals of approximately 1.48 ms. Fig. 6a illustrates the estimated velocity vector field (radial component u_r) based on Eq. (2) for $T = t_1$ in Case 1.

Therefore, to summarize the analysis conducted up until here, increasing the pressure inside the compressed air system leads to greater values of the upward velocity and acceleration of the top disk. As a consequence, increasingly stronger non-uniform jets form in the gap between the disks, which is the underlying mechanism for two counter-rotating vortices. This effect arises because the axes of the disks are not perfectly aligned, but are positioned at an imperceptibly small angle. Consequently, a circumferential inhomogeneity develops in the flow entering the gap between the disks. In contrast, the negative squeeze film theory models the flow behavior under conditions of uniformity, assuming perfectly aligned disks.

3.3. An explanation for the entry jet

When the two disks are in contact, a vertical force equivalent to or larger than the stiction force should be applied to the top disk to separate it from the bottom one. We assume that the stiction force is

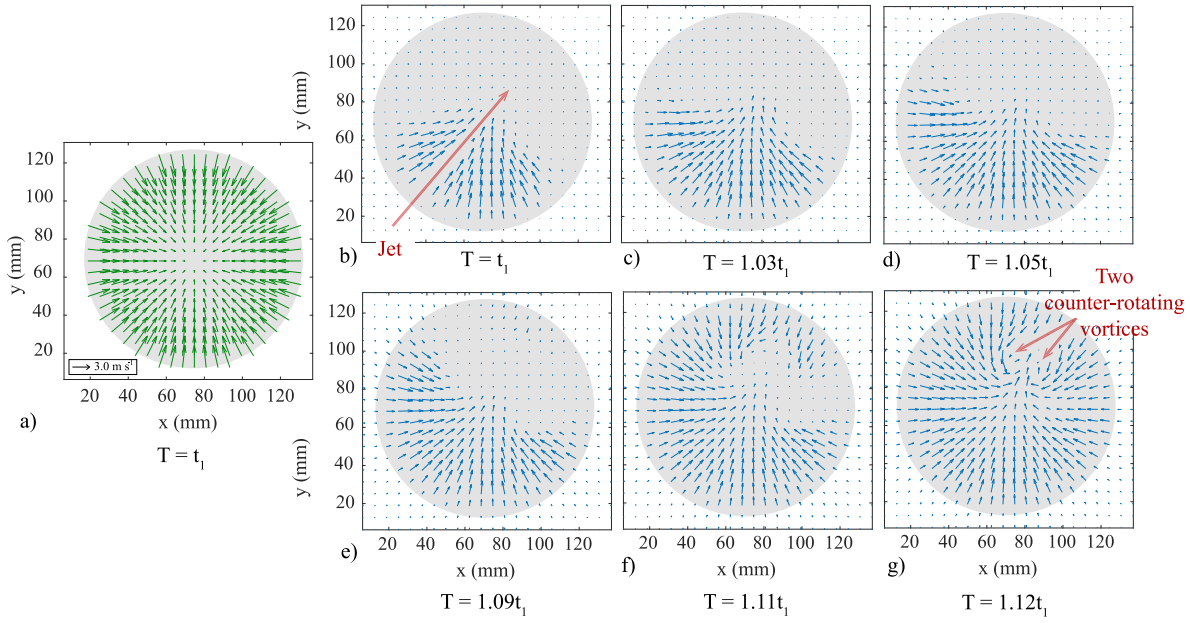

Fig. 6. (a) Velocity vector field based on the negative squeeze film theory as defined by Eq. (2). (b) to (g) Formation of the two counter-rotating vortices due to non-uniform flow in the radial direction (jet). The laser sheet is aligned parallel to the disks, and is located about 3.6 mm above the bottom disk. The case displayed here to illustrate the generation of the vortices is a non-cavitating one (Case 1).

F and that a negligibly small misalignment $\alpha \ll 1$ exists between the disk and the axis of movement. Then, to separate the top disk from the bottom disk a force should be applied along the axis of movement of the top disk, such that its component orthogonal to the plane of the two disks is equivalent to or larger than F. This force will also have a component parallel to the disks of αF, as illustrated in Fig. 7a. While to vertically displace the top disk the stiction force should be overcome, a much smaller horizontal force would be sufficient to slide the disk laterally. This difference arises primarily from hydrodynamic and adhesive forces (Nagy, 2024) present in the thin water film between the disks. As a result, the rise of the top disk is combined with its horizontal movement, which determines an azimuthally non-uniform radial pressure gradient, at the origin of the observed entry jet. Note in Fig. 7 that the top disk moves upward, while it also slides horizontally.

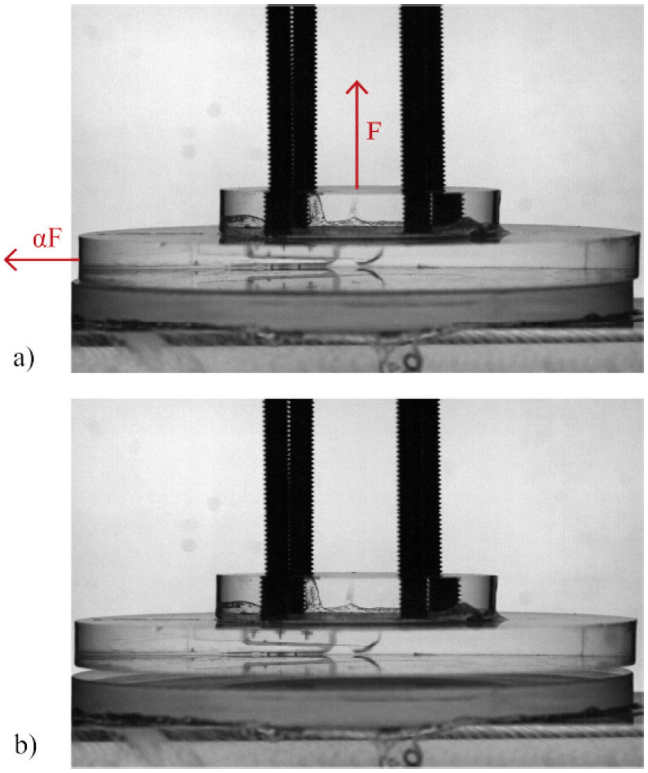

Fig. 7. Photo (a) shows the initial condition of the disks, and photo (b) exhibits the vertical and horizontal movement of the top disk.

3.4. Comparison between experimental non-uniform velocity and theoretical uniform velocity

The comparison of velocity profiles is performed between experimental results, involving non-uniform circumferential inflow, and theoretical predictions, calculated under the hypothesis of uniform inflow. This analysis allows for the evaluation of similarities and discrepancies in the effects of the non-uniform flow in experimental conditions versus uniform flow in idealized theoretical assumptions. For this purpose, the solution from negative squeeze film theory is employed, which provides an analytical solution for estimating the radial velocity of the flow entering the gap, u_r. This estimation is based on the velocity of the moving disk, the gap height between the disks, and the measurement position z, see Eq. (2). Given that the laser is positioned approximately 3.6 mm above the fixed bottom disk, this value is used as the height z in the equation to estimate the radial velocity.

Fig. 8a presents a comparison between the experimental and analytical velocities. The experimental velocity is determined by calculating the radial velocity near the edges of the disks, which are taken between angles of 120° and 360° with respect to the counterclockwise angle convention. This region is specifically selected to minimize the influence of the vortices on the radial velocity near the disk edges. Fig. 8b demonstrates that the velocity profile is nonlinear with respect to the radius, in contrast to what is suggested by Eq. (2). The flow exhibits high velocity upon entering the gap between the disks, followed by a reduction in velocity, a characteristic consistent with a *vena contracta* type of acceleration produced by the constricted gap, similar to the behavior observed in nozzle flows (Hashiehbaf and Romano, 2013). It is important to note that the analytical solution represents an idealized

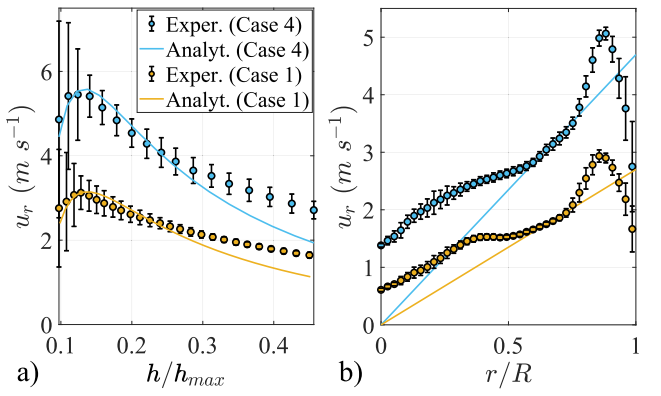

Fig. 8. Experimental and analytical radial velocity u_r comparison (a) when fixing the radius r and varying the gap height between the disks h, and (b) when fixing h and varying r. The value of the fixed radius used for the graph is 5.76 mm and the value of the fixed gap height is 10.6 mm. The error bars indicate the standard deviation of the radial velocity when varying its angular position.

case, where the velocity is perfectly axi-symmetric and goes to zero at $r = 0$. In the experimental results, however, the radial velocity is associated with an entry jet (see Fig. 6), which is produced by a non-uniform pressure distribution in the gap between the two disks.

In conclusion, the theoretical and experimental radial velocities show good agreement, with a RMSE of 0.2679 m s^{-1} and 0.4322 m s^{-1} for Case 1 and Case 4, respectively (Fig. 8a).

3.5. Cavitation number

The definition of the cavitation number for non-conventional problems, such as the one analyzed in this paper, can be a non-trivial aspect. For this reason, different possible definitions of the cavitation number are discussed in this section. As described by Franc and Michel (2005), the cavitation number for a foil in a cavitation tunnel can be formulated as:

$$\sigma = \frac{p_r - p_v}{\frac{1}{2}\rho V^2} \tag{8}$$

where p_r is a reference pressure and V is a velocity that characterizes the system, typically the free-stream velocity under steady-state conditions, which is a global parameter.

In the current study, the flow is transient, with the entire phenomenon occurring within tens of milliseconds, which makes it difficult to define representative values for pressure and velocity to be used in the aforementioned definition of the cavitation number. One possible choice for the characteristic velocity for the cavitation number is the instantaneous maximum azimuthal vortex velocity at inception.

In the present problem, it can be observed that prior to the movement of the disk, the liquid is quiescent. A type of cavitation in static liquids under transient flow conditions has been investigated by Daily et al. (2014), Garcia-Atance Fatjo (2016), and Pan et al. (2017). In these studies, cavitation arises due to impulsive forces generated by sudden accelerations in the liquid. The authors propose a potential dimensionless number that captures cavitation onset due to acceleration, expressed as

$$\sigma = \frac{p_r - p_v}{\rho a L_c}, \tag{9}$$

where a is the acceleration and L_c is a characteristic length. According to their findings, cavitation occurs when the cavitation number is less than 1; otherwise, it does not occur. Additionally, these studies note that sudden accelerations typically occur within a time frame of less than 4 ms, and the cavitation onset and collapse span approximately 7 ms in total. Therefore, a possible cavitation number for the problem under investigation is shown in Eq. (9), where the maximum acceleration is 96 m s^{-2}, see Table 1, and the disk diameter is taken as characteristic length, L_c.

Table 4
Different values of the cavitation number for Case 4 obtained by following three possible definitions.

Definition	Characteristic flow property	Value of characteristic flow property	Cavitation number, σ
Eq. (8)	max azimuthal velocity vortices	8.24 m s^{-1}	2.94
Eq. (9)	max acceleration top disk	96 m s^{-2}	8.60
Eq. (10)	max velocity entry jet	12.26 m s^{-1}	1.33

As discussed earlier, cavitation tunnels typically use the free-stream velocity as the global characteristic velocity for estimating the cavitation number. An additional possible velocity to define the cavitation number is the jet velocity when the disks first separate. The following relationship is therefore proposed for the estimation of the cavitation number

$$\sigma = \frac{p_{atm} + \rho g H - p_v}{\frac{1}{2}\rho u_r^2}, \tag{10}$$

where p_{atm} is the atmospheric pressure, H is the height of the water column and u_r is the radial velocity near the edge of the disk.

Since the PIV recordings are constrained by the position of the laser sheet, and the radial velocity u_r calculated using Eq. (2) exhibits good agreement with the experimental radial velocity (see Fig. 8), the same equation, i.e. Eq. (2), can be applied to determine the characteristic flow velocity for the cavitation number. Note that for Fig. 8, z is fixed in Eq. (2) due to the position of the laser. Thus, the maximum radial velocity is captured at the initial moment of disk separation and $z = h/2$. This requires estimating the limit of h and $\dot{h}$ in Eq. (5) and (6), respectively, as time t tends to zero. These results are then used to compute the radial velocity u_r in Eq. (10), ensuring that the initial flow velocity is accurately reflected in the cavitation number estimation.

Table 4 shows the estimates of three possible cavitation numbers, each of them defined using different characteristic flow properties, depending on the chosen definition of the cavitation number. These characteristic flow properties are (i) the maximum instantaneous azimuthal velocity of the vortices at inception, (ii) the maximum acceleration of the top disk, as expressed in Eq. (9), and (iii) the estimated initial jet velocity when water first enters the gap between the disks, given by Eq. (10). Note that $p_r = p_{atm} + \rho g H$ for Eqs. (8) and (9).

In the present work, the formation of cavitating vortices seems to be due to high local velocities in the flow rather than sudden acceleration. As seen in Fig. 4c, by the time the highest acceleration is reached, the cavitating vortices have already formed, as illustrated in Fig. 3o and 3u. This emphasizes the role of local flow velocities in the cavitation process. Additionally, the cavitation number based on the acceleration yields values significantly greater than 1, despite the observed occurrence of cavitation.

Regarding the cavitation numbers defined by flow velocities, two options are evaluated, both showing similar values and lower cavitation numbers compared with the value obtained using acceleration. The first option is an instantaneous local velocity, which can only be measured using techniques that provide spatially resolved velocity fields. In addition, two vortices are formed, raising the question of which vortex should be selected for determining this characteristic velocity. The second option is the jet velocity at the moment the disks first separate. This latter velocity can be estimated using the analytical expression for the radial velocity given in Eq. (2).

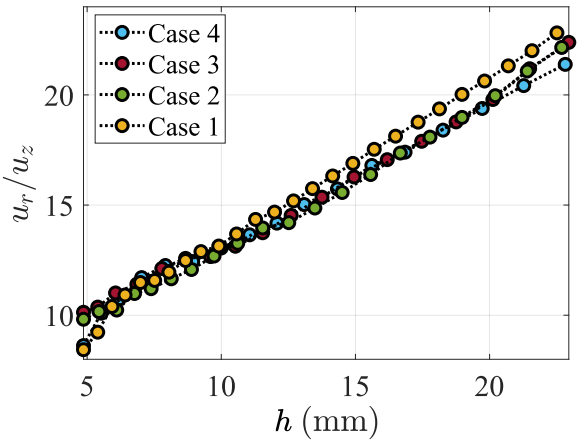

Fig. 9. Ratio between the radial velocity and the estimated vertical velocity for the four cases as a function of the gap height h between the two disks.

Therefore, in summary, three possible definitions of cavitation number are evaluated to identify which, if any, can describe the physical behavior of the present transient flow. The definition of cavitation number based on acceleration, while relevant for impulsive cavitation in quiescent liquids, is unsuitable in this case. Cavitation appears before the peak acceleration is reached and the associated cavitation number is significantly greater than 1. In contrast, the definitions based on velocity, either the instantaneous maximim vortex velocity or the estimated initial jet velocity, yield lower values that are more consistent with the observed onset of cavitation. However, from these definitions, no specific characteristic flow property provides a fully representative cavitation number for the problem studied here, thus emphasizing the impossibility of unequivocally defining the cavitation number in the transient and complex flow under investigation.

3.6. Can the vertical component of the flow velocity be neglected?

The experiments presented here focus on measuring the velocity in a specific plane, corresponding to the laser position, which is parallel to the disks. This laser positioning is selected to capture the radial flow as it initially enters the gap between the disks using PIV recordings. The pressure reconstruction is performed during the inception of cavitation, which occurs at the beginning of disk separation. At this early stage, the flow is expected to be predominantly radial, and the pressure reaches its lowest point. As the gap between the disks increases, the vertical velocity is expected to start influencing the flow, as well as the pressure is expected to rise.

In Fig. 9, the ratio between the radial velocity and the estimated vertical velocity of the flow is displayed. The vertical velocity is calculated by Eq. (3), where z is the laser sheet's position within the gap. This estimation evidences that the vertical velocity component is not expected to significantly impact the pressure reconstruction when compared to the horizontal velocity components (x and y directions), because the radial velocity is one order of magnitude higher than the vertical velocity.

3.7. PIV data and pressure reconstruction

The velocity field computed by PIV allows for pressure reconstruction, which is essential for a deeper understanding of the flow phenomena. Moreover, the vorticity field of the vortex pair provides further insight into the characteristics of the two vortices at the different time instants.

Fig. 10 emphasizes the asymmetric behavior of the vortex pair. The displacement of the vortex core from Fig. 10a, 10e, 10i and 10m compared to Fig. 10d, 10h, 10l and 10p respectively, are summarized in Table 5. For the non-cavitating vortices, the displacements of both vortices are similar. However, in the cavitating cases, the displacement of the right vortex is significantly lower compared to the left vortex, highlighting the greater strength of the right one.

Table 5
The displacement of the left and right vortex core for the four cases for the gap height between the disks of 4.9 mm and 22.7 mm.

	Displacement of Left Vortex (mm)	Displacement of Right Vortex (mm)
Case 1	12.67	14.30
Case 2	8.27	4.54
Case 3	8.87	1.56
Case 4	11.01	2.81

The velocity vectors and vorticity fields depicted in Fig. 10 are presented at the same scale, facilitating the comparison between the cases. As expected, the vortices exhibit the lowest vorticity values in the non-cavitating case. A noteworthy observation is that the right vortex moves less than the left one, as seen in Fig. 10h, 10l, and 10p. However, in the non-cavitating case (Case 1), the vortices exhibit similar movement patterns; see Fig. 10d.

To give further support to the hypothesis that the origin of the observed bubbles is cavitation, the pressure field is reconstructed from PIV data in the region where the vortices occur. Simplifying assumptions defined in Section 2.3 to the Navier–Stokes equations are introduced, and a Poisson solver is applied. In order to evaluate the necessary number of iterations to reach convergence, the value of minimum pressure inside both vortices as a function of the number of iterations of the Poisson solver is examined, and convergence is reached after 10^4 iterations. The estimated pressure fields for Case 4 and Case 1 are presented in Fig. 11, respectively Fig. 11a and 11b, where the velocity vector field is also depicted. It is important to mention that the velocity field shown in Fig. 11 is obtained from the image oversampling of ten repetitions (Samarage et al., 2012). The absolute pressure in the core of the right vortex in Fig. 11a is 2.26 kPa, i.e., lower than the vapor pressure, with the latter being 2.65 kPa for the experimental conditions. This represents an additional important indication that a phase transition occurs at the core of the vortices in Case 4. In Fig. 11b, where the velocity field and pressure distribution for the non-cavitating case are presented, the pressure inside the vortex is 82.63 kPa for the left vortex and 84.62 kPa for the right vortex, therefore much larger than the vapor pressure.

The window size used to process the particle images significantly influences the results of the pressure reconstruction. Smaller window sizes yield more precise results, but also increase random errors. Consequently, reducing the window size allows for higher spatial resolution, which helps to better resolve the pressure within the vortices. This effect is illustrated in Fig. 12, where a notable impact on the pressure inside the vortex core is observed when the window size decreases from 64 × 64 px to 32 × 32 px. The pressure reduction becomes even more pronounced when further decreasing the window size from 64 × 64 px to 8 × 8 px, particularly for the lowest pressure value in Case 4. However, further reduction of the window size below 8 × 8 px is undesirable due to increased errors. As expected, the 64 × 64 px window size curve is smoother compared to other cases, owing to the smoothing effect of having a larger window size.

By performing correlation averaging and applying a Poisson solver for different instants for all cases, a graph of the lowest pressure value inside the vortex cores, p_{min}, as a function of the gap height between the two disks can be plotted (Fig. 13). The development of the vortices and their onset to cavitation, which we have thus far illustrated from shadowgraphy images (Fig. 3), can here be interpreted in relation to the variation of the minimum pressure inside the cores of the vortices. Notably, the lowest pressure values within the left vortex core are

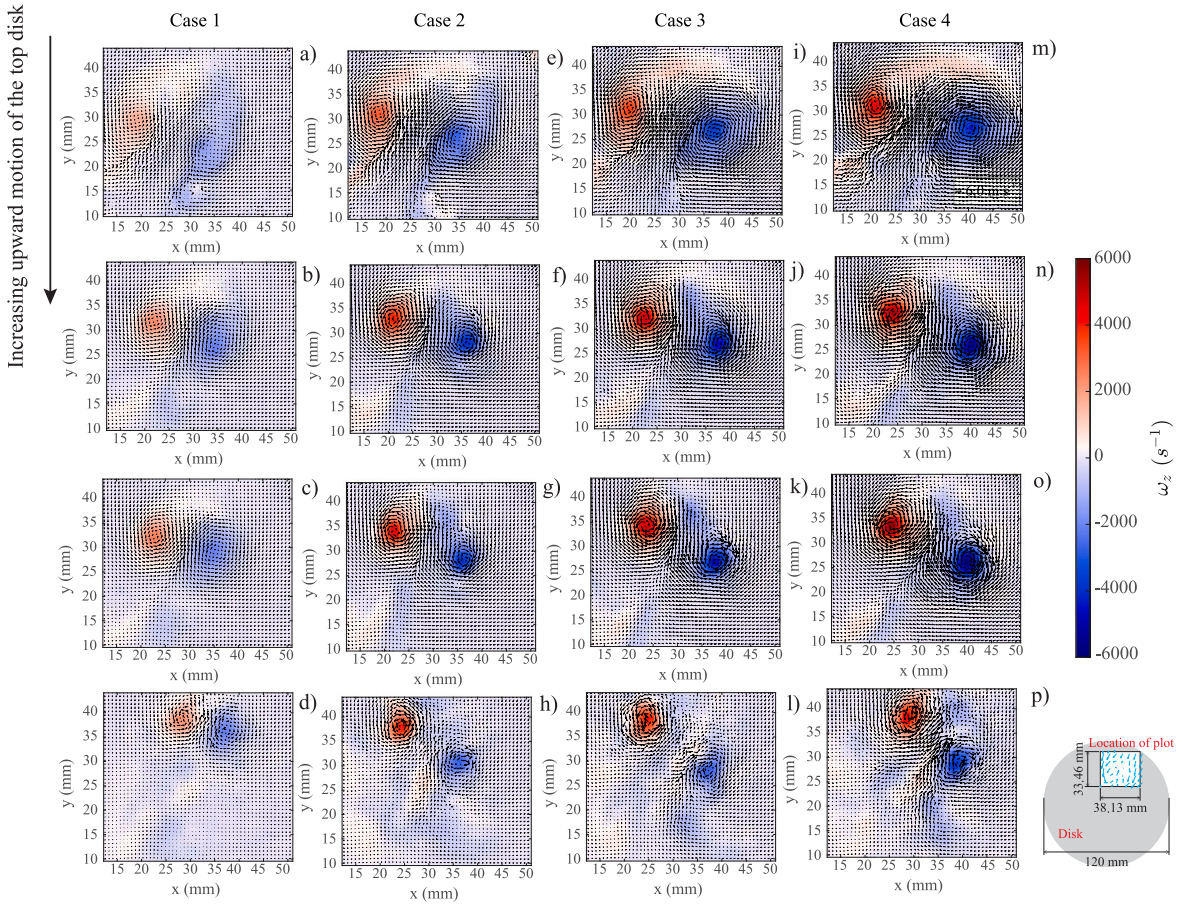

Fig. 10. The vorticity field and velocity vector fields are illustrated for the four cases at four distinct heights between the disks h, specifically at 4.9 mm, 8.9 mm, 11.2 mm, 22.7 mm. The figure on the bottom right represents where the vortices form in relation to the disk.

higher than the vapor pressure. This could be attributed to insufficient spatial resolution or water quality effect. In the cavitating cases, the bubbles trapped within the left vortex gradually increase in size as the minimum pressure decreases.

The minimum pressure, p_{min}, estimated analytically using Eq. (4), is shown in Fig. 13. According to the negative squeeze film theory, the lowest pressure occurs at the center of the disk $r = 0$, which is the reference point for the analytical estimation presented in Fig. 13. The results indicate that the analytically calculated pressure does not drop below the vapor pressure, confirming that cavitation is driven by the non-uniform flow responsible for generating the two counter-rotating vortices.

Data are resampled without correlation averaging to evaluate the standard deviation of the pressure reconstruction from the PIV images. The standard deviation is calculated according to Coleman and Steele (2009) for ten repetitions with a 95% confidence interval and a Student's t distribution of 2.262. This is represented by the error bars in Fig. 13.

To assess whether the left vortex in Case 4 statistically reaches pressures below the vapor pressure, the standard deviation was calculated for all available data points. This analysis was performed only for Case 4 for two reasons. The first reason is that this is the case in which the minimum pressure comes closest to the vapor pressure. And the second reason is that obtaining each minimum pressure value requires completing both the PIV analysis and the pressure reconstruction for every experimental repetition, totaling 810 individual computations. The results show that the average standard deviation is 5.46 kPa for the left vortex and 5.65 kPa for the right vortex. The lowest pressure measured for the left vortex is 8.92 kPa. Therefore, even when accounting for the associated uncertainty, the pressure in the left vortex does not statistically reach values below the vapor pressure.

For Case 3 and 4, where both cavitating vortices appear, the observation obtained from shadowgraphy, i.e. that the onset of cavitation is abrupt for the right vortex if compared to the left one, can here be explained by the relatively lower values of pressure of the right vortex (Fig. 13). This pressure difference could be attributed to the initial sliding motion proposed in Fig. 7, which leads to a different formation process for the two vortices. Consistently, the left cavitating vortex always forms more slowly than the right one.

4. Conclusions

This study explored the flow in the gap between two coaxial disks, where the top disk was brought into rapid diverging movement after being initially in contact with the bottom one. The vertical displacement of the top disk led to a radial non-uniform inflow of quiescent external fluid, which determined an entry jet flow in the thin film between the disks. This was associated to the formation of two counter-rotating vortices, which, in some cases, exhibited gaseous cores, observed in our experiments of high-speed shadowgrahy. To assess whether such gaseous cores were the result of cavitation, pressure was reconstructed from velocity fields obtained from 2D-PIV, which was performed in a plane orthogonal to the axis of the disks, a few millimeters above the bottom disk. The reconstructed pressure was found to be highly sensitive to the spatial resolution of the velocity vector fields. For this reason, a sum-of-correlation algorithm was applied. From this analysis, the local pressure inside the core of the right vortex was found to be

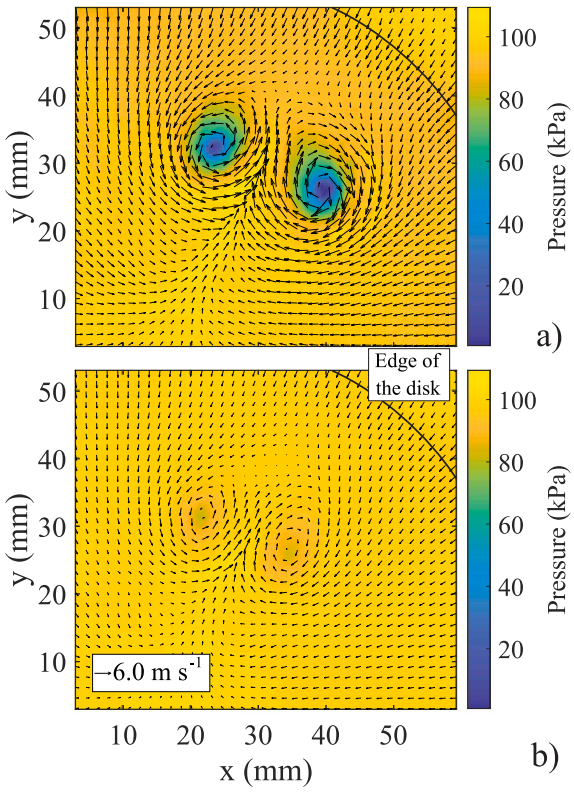

Fig. 11. Velocity vector fields as reconstructed from PIV and sum of correlation, and pressure fields obtained from the velocity data at h = 8 mm for Case 4 in (a), and Case 1 in (b). The pressure fields are computed with a 8 × 8 px window size and a 50% window overlapping. For clarity, only every 8th velocity vector from the PIV result is shown.

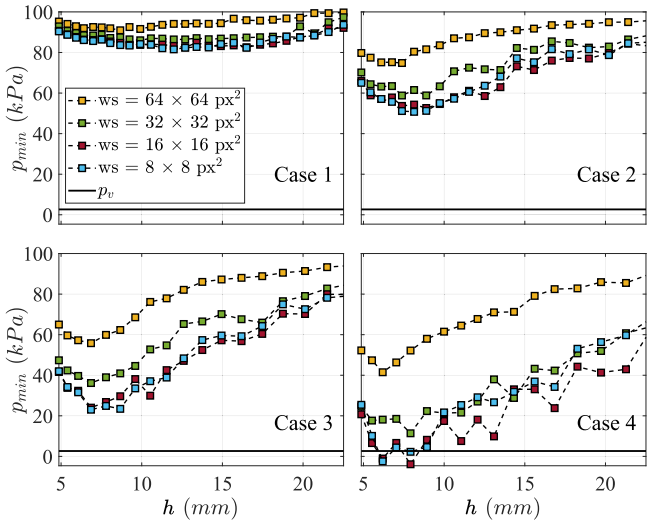

Fig. 12. The impact of window size on the pressure reconstruction is assessed for the four cavitation numbers and for the right vortex.

lower than the vapor pressure for relatively high values of velocity and acceleration of the top disk, thus clearly evidencing that cavitation could be accounted for as responsible for the gaseous vortex cores.

From the aforementioned experimental analyses, the time-dependent flow topology was thoroughly characterized. While the vortices for the non-cavitating case presented nearly identical vorticity as the mutual gap height between the disks grows, cavitating vortices showed different behaviors, also in relation to minimum core pressure. In particular, the left vortex (rotating counterclockwise) strengthened gradually as the top disk raised, whereas the right vortex (rotating clockwise) often experienced abrupt cavitation onset and sudden collapse. This could be attributed to the sliding motion proposed in Fig. 7, which leads to a more abrupt formation of the right vortex compared with the left one. In addition, bubbles in the left vortex gradually increase in size, leading to the formation of a cavity, while those in the right vortex remain relatively unchanged, with cavitation inception occurring suddenly. Furthermore, in cavitating cases, the right vortex was observed to move comparatively much less than the left vortex as the disk gap increases.

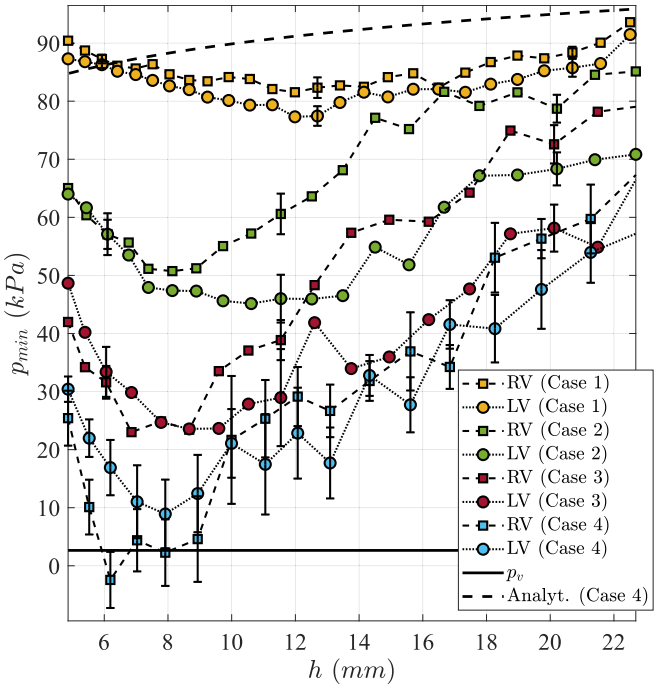

Fig. 13. Time evolution of lowest pressure in the core, p_{min}, of the two vortices, as a function of the gap height between the two disks. The analytical solution is estimated at r = 0, where the pressure is known for its lower value.

Fig. 14 summarizes the formation process of the non-uniform entry jet that arises from the way in which the two disks separate. The fact that the vortices appear at the location of the last point of contact between the disks is not coincidental. At this location, flows with different velocities meet, generating shear that naturally rolls up into a pair of counter-rotating vortices. The non-dimensionalized time, defined with respect to the instant when the moving disk reaches its final position (see Table 1), is also shown in Fig. 14 for the two cases in which two cavitating vortices appear, i.e. Case 3 and Case 4.

An analytical solution for the flow was calculated by applying the negative squeeze film theory. A comparison between the pressure from this analytical model and the pressure reconstructed from velocity data revealed that the analytical model dramatically overestimates the minimum pressure in the flow, thus largely failing to predict the onset of cavitation. This is because an azimuthally uniform inflow cannot capture the formation of the counter-rotating vortices, which is key in confidently modeling the onset of cavitation in problems of tribonucleation. In fact, in reality, the two disks would never be perfectly parallel as they are expected to be in the analytical model, which leads to the formation of *i.* the entry jet, *ii.* the counter-rotating vortices, and *iii.* the associated low-pressure regions, each of which we observed in our experiments. This makes the negative squeeze film

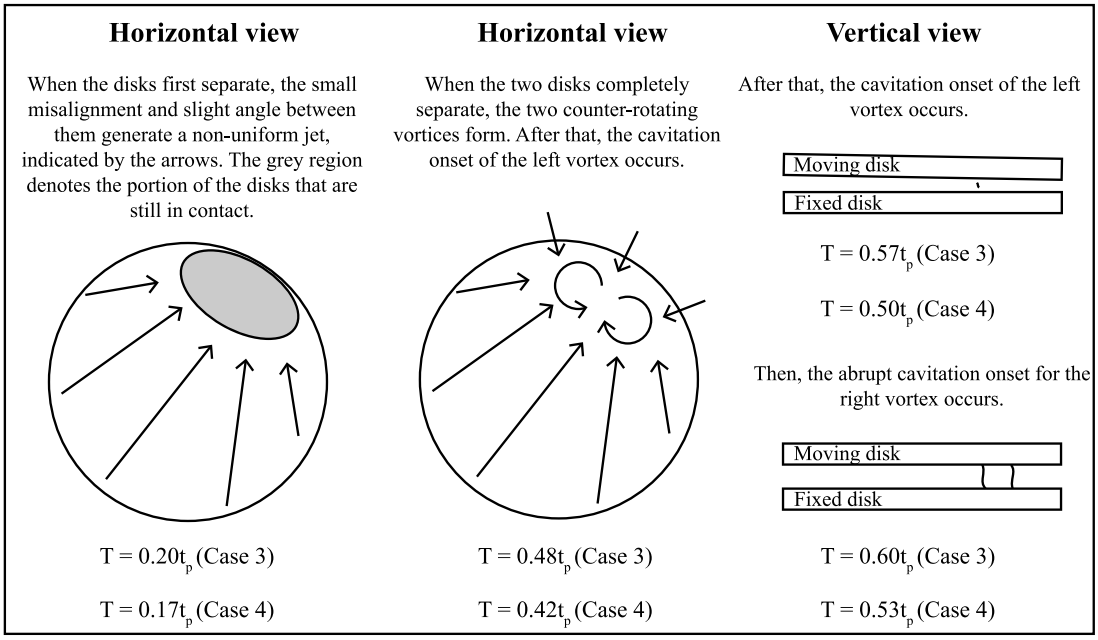

Fig. 14. Conceptual schematic showing how the non-uniform inflow leads to the formation of two counter-rotating vortices at the point of last contact between the disks, as well as the subsequent onset of cavitation.

theory inadequate to predict cavitation in this flow, for thin films of a few millimeters and larger. Despite this, when comparing the radial velocities from experimental result and analytical solution, we found fairly small deviations, which indicated that the analytical model still represents a valuable tool in estimating the radial velocity in the film.

CRediT authorship contribution statement

Mariana Costa: Writing – original draft, Visualization, Methodology, Investigation, Formal analysis. **Tom van Terwisga:** Supervision, Funding acquisition. **Daniele Fiscaletti:** Writing – review & editing, Writing – original draft, Supervision. **Jerry Westerweel:** Writing – review & editing, Supervision, Software, Funding acquisition, Formal analysis.

Declaration of competing interest

The authors declare the following financial interests/personal relationships which may be considered as potential competing interests: Mariana Costa reports financial support was provided by Nederlandse Organisatie voor Wetenschappelijk Onderzoek. If there are other authors, they declare that they have no known competing financial interests or personal relationships that could have appeared to influence the work reported in this paper.

Acknowledgments

We acknowledge Renée van Zanten, under the supervision of Dr. Peter Wellens, for their preliminary contributions to this research. We also thank Mallaury Lambrechts for her support with data collection. We finally thank Edwin Overmars for his invaluable advice, assistance and help.

This publication is part of the CAV-1 project (project number P17-07) of the research program Water Quality in Maritime Hydrodynamics (AQUA), which is funded by the Dutch Research Council (NWO). The support by NWO and project partners is gratefully acknowledged.

Appendix A. Supplementary data

Supplementary material related to this article can be found online at https://doi.org/10.1016/j.ijmultiphaseflow.2026.105635.

Data availability

Data will be made available on request.

References

Adhikari, U., Goliaei, A., Berkowitz, M.L., 2016. Nanobubbles, cavitation, shock waves and traumatic brain injury. Phys. Chem. Chem. Phys. 18 (48), 32638–32652. http://dx.doi.org/10.1039/C6CP06704B.

Arndt, R.E.A., 1981. Cavitation in fluid machinery and hydraulic structures. Annu. Rev. Fluid Mech. 13 (1), 273–326. http://dx.doi.org/10.1146/annurev.fl.13.010181.001421.

Braun, M.J., Hannon, W.M., 2010. Cavitation formation and modelling for fluid film bearings: A review. Proc. Inst. Mech. Eng. Part J: J. Eng. Tribol. 224 (9), 839–863. http://dx.doi.org/10.1243/13506501JET772.

Chandran Suja, V., Barakat, A.I., 2018. A mathematical model for the sounds produced by knuckle cracking. Sci. Rep. 8 (1), 4600. http://dx.doi.org/10.1038/s41598-018-22664-4.

Chen, Y.L., Israelachvili, J., 1991. New mechanism of cavitation damage. Science 252 (5009), 1157–1160. http://dx.doi.org/10.1126/science.252.5009.1157.

Coleman, H.W., Steele, W.G., 2009. Experimentation, Validation, and Uncertainty Analysis for Engineers, first ed. Wiley, http://dx.doi.org/10.1002/9780470485682.

Combriat, T., Dysthe, D.K., Flekkøy, E.G., 2024. Cavitation dynamics in creeping flow. J. Fluid Mech. 999, A19. http://dx.doi.org/10.1017/jfm.2024.937.

Daily, J., Pendlebury, J., Langley, K., Hurd, R., Thomson, S., Truscott, T., 2014. Catastrophic cracking courtesy of quiescent cavitation. Phys. Fluids 26 (9), 091107. http://dx.doi.org/10.1063/1.4894073.

Erinin, M.A., Néel, B., Mazzatenta, M.T., Duncan, J.H., Deike, L., 2023. Comparison between shadow imaging and in-line holography for measuring droplet size distributions. Exp. Fluids 64 (5), 96. http://dx.doi.org/10.1007/s00348-023-03633-8.

Ertas, B., Delgado, A., 2018. Hermetically sealed squeeze film damper for operation in oil-free environments. In: Structures and Dynamics, vol. 7B, American Society of Mechanical Engineers, Oslo, Norway, http://dx.doi.org/10.1115/GT2018-76308, V07BT34A035.

Franc, J.P., Michel, J.M., 2005. Fundamentals of Cavitation. Fluid Mechanics and Its Applications, vol. 76, Springer Netherlands, Dordrecht, http://dx.doi.org/10.1007/1-4020-2233-6,

Garcia-Atance Fatjo, G., 2016. New dimensionless number to predict cavitation in accelerated fluid. Int. J. Comput. Methods Exp. Meas. 4 (4), 484–492. http://dx.doi.org/10.2495/CMEM-V4-N4-484-492.

Geike, T., 2020. Review on the bubble dynamics based cavitation dynamics for the negative squeeze motion in lubricated contacts. Front. Mech. Eng. 6, 33. http://dx.doi.org/10.3389/fmech.2020.00033.

Ghasemnezhad, M., Roohi, E., 2024. Large eddy simulation of cavitating flow around a pitching hydrofoil. Ocean Eng. 292, 116547. http://dx.doi.org/10.1016/j.oceaneng.2023.116547.

Hashiehbaf, A., Romano, G., 2013. Particle image velocimetry investigation on mixing enhancement of non-circular sharp edge nozzles. Int. J. Heat Fluid Flow 44, 208–221. http://dx.doi.org/10.1016/j.ijheatfluidflow.2013.05.017.

Hele-Shaw, H.S., 1898. The flow of water. Nature 58 (1489), 34–36. http://dx.doi.org/10.1038/058034a0.

Hori, Y., 2006. Hydrodynamic Lubrication. Springer, Hicom, Japan, original-date: 2002.

Kawchuk, G.N., Fryer, J., Jaremko, J.L., Zeng, H., Rowe, L., Thompson, R., 2015. Real-time visualization of joint cavitation. In: Zhang, Q. (Ed.), PLoS ONE 10 (4), e0119470. http://dx.doi.org/10.1371/journal.pone.0119470.

Kelly, R., Goldstein, D.B., Suryanarayanan, S., Botto Tornielli, M., Handler, R.A., 2021. The nature of bubble entrapment in a Lamb–Oseen vortex. Phys. Fluids 33 (6), 061702. http://dx.doi.org/10.1063/5.0053658.

Konrath, R., Schröder, W., 2002. Telecentric lenses for imaging in particle image velocimetry: a new stereoscopic approach. Exp. Fluids 33 (5), 703–708. http://dx.doi.org/10.1007/s00348-002-0531-7.

Kurosawa, Y., Kato, K., Saito, S., Kubo, M., Uzuka, T., Fujii, Y., Takahashi, H., 2009. Basic study of brain injury mechanism caused by cavitation. In: 2009 Annual International Conference of the IEEE Engineering in Medicine and Biology Society. pp. 7224–7227. http://dx.doi.org/10.1109/IEMBS.2009.5335260.

Lang, J., Nathan, R., Wu, Q., 2019. Experimental study of transient squeezing film flow. J. Fluids Eng. 141 (8), 081110. http://dx.doi.org/10.1115/1.4042758.

Meinhart, C.D., Wereley, S.T., Santiago, J.G., 2000. A PIV algorithm for estimating time-averaged velocity fields. J. Fluids Eng. 122 (2), 285–289. http://dx.doi.org/10.1115/1.483256.

Melissaris, T., Schenke, S., Bulten, N., Van Terwisga, T.J., 2020. On the accuracy of predicting cavitation impact loads on marine propellers. Wear 456–457, 203393. http://dx.doi.org/10.1016/j.wear.2020.203393.

Moffatt, H., Guest, H., Huppert, H.E., 2021. Spreading or contraction of viscous drops between plates: single, multiple or annular drops. J. Fluid Mech. 925, A26. http://dx.doi.org/10.1017/jfm.2021.668.

Nagy, N., 2024. Determination of solid-liquid adhesion work on flat surfaces in a direct and absolute manner. Sci. Rep. 14 (1), 29991. http://dx.doi.org/10.1038/s41598-024-81710-6.

Pan, Z., Kiyama, A., Tagawa, Y., Daily, D.J., Thomson, S.L., Hurd, R., Truscott, T.T., 2017. Cavitation onset caused by acceleration. Proc. Natl. Acad. Sci. 114 (32), 8470–8474. http://dx.doi.org/10.1073/pnas.1702502114.

Pennings, P.C., Westerweel, J., Van Terwisga, T.J.C., 2015. Flow field measurement around vortex cavitation. Exp. Fluids 56 (11), 206. http://dx.doi.org/10.1007/s00348-015-2073-9.

Poivet, S., Nallet, F., Gay, C., Fabre, P., 2003. Cavitation-induced force transition in confined viscous liquids under traction. Eur. Lett. (EPL) 62 (2), 244–250. http://dx.doi.org/10.1209/epl/i2003-00352-3.

Resch, M., Scheidl, R., 2014. A model for fluid stiction of quickly separating circular plates. Proc. Inst. Mech. Eng. Part C: J. Mech. Eng. Sci. 228 (9), 1540–1556. http://dx.doi.org/10.1177/0954406213509613.

Reynolds, O., 1886. IV. On the theory of lubrication and its application to Mr. Beauchamp tower's experiments, including an experimental determination of the viscosity of olive oil. Philos. Trans. R. Soc. Lond. 177, 157–234. http://dx.doi.org/10.1098/rstl.1886.0005.

Roemer, D.B., Johansen, P., Pedersen, H.C., Andersen, T.O., 2015. Fluid stiction modeling for quickly separating plates considering the liquid tensile strength. J. Fluids Eng. 137 (6), 061205. http://dx.doi.org/10.1115/1.4029683.

Saffman, P.G., Taylor, G.I., 1958. The penetration of a fluid into a porous medium or Hele-Shaw cell containing a more viscous liquid. Proc. R. Soc. Lond. Ser. A. Math. Phys. Sci. 245 (1242), 312–329. http://dx.doi.org/10.1098/rspa.1958.0085.

Samarage, C.R., Carberry, J., Hourigan, K., Fouras, A., 2012. Optimisation of temporal averaging processes in PIV. Exp. Fluids 52 (3), 617–631. http://dx.doi.org/10.1007/s00348-011-1080-8.

Scheidl, R., Gradl, C., 2016. An approximate computational method for the fluid stiction problem of two separating parallel plates with cavitation. J. Fluids Eng. 138 (6), 061301. http://dx.doi.org/10.1115/1.4032299.

Sciacchitano, A., Scarano, F., 2014. Elimination of PIV light reflections via a temporal high pass filter. Meas. Sci. Technol. 25 (8), 084009. http://dx.doi.org/10.1088/0957-0233/25/8/084009.

Sobhi, S., El Khlifi, M., Nabhani, M., 2023. Effects of both cavitation and non-Newtonian behavior on the performance of oscillatory anisotropic poroelastic squeeze film. Ind. Lubr. Tribol. 75 (2), 145–156. http://dx.doi.org/10.1108/ILT-08-2022-0238.

Stefan, J., 1875. Versuche über die scheinbare Adhäsion. Ann. Phys., Lpz. 230 (2), 316–318. http://dx.doi.org/10.1002/andp.18752300213.

Thielicke, W., Stamhuis, E.J., 2014. PIVlab – towards user-friendly, affordable and accurate digital particle image velocimetry in MATLAB. J. Open Res. Softw. 2, http://dx.doi.org/10.5334/jors.bl.

Unsworth, A., Dowson, D., Wright, V., 1971. 'Cracking joints'. A bioengineering study of cavitation in the metacarpophalangeal joint. Ann. Rheum. Dis. 30 (4), 348–358. http://dx.doi.org/10.1136/ard.30.4.348.

Versluis, M., Schmitz, B., Von Der Heydt, A., Lohse, D., 2000. How snapping shrimp snap: through cavitating bubbles. Science 289 (5487), 2114–2117. http://dx.doi.org/10.1126/science.289.5487.2114.

Wang, Y., Feng, Z., Frechette, J., 2020. Dynamic adhesion due to fluid infusion. Curr. Opin. Colloid Interface Sci. 50, 101397. http://dx.doi.org/10.1016/j.cocis.2020.101397.

Westerweel, J., Geelhoed, P.F., Lindken, R., 2004. Single-pixel resolution ensemble correlation for micro-PIV applications. Exp. Fluids 37 (3), 375–384. http://dx.doi.org/10.1007/s00348-004-0826-y.

Yoshizumi, F., Kondoh, Y., Moroi, T., Tamano, S., Morinishi, Y., 2018. Model study on the oil stiction of a discharge reed valve in compressors. J. Tribol. 140 (2), 021103. http://dx.doi.org/10.1115/1.4037539.